The Effect of Reynolds Number on the Hypersonic Flow around Faceted Shapes

Conference Paper · September 2018

DOI: 10.2514/6.2018-5197

3 authors, including:

Thomas Rees
TOffeeAM Ltd.
8 PUBLICATIONS **25** CITATIONS
SEE PROFILE

Jim A. Merrifield
Fluid Gravity Engineering Ltd
68 PUBLICATIONS **287** CITATIONS
SEE PROFILE

The Effect of Reynolds Number on the Hypersonic Flow around Faceted Shapes

Thomas W. Rees* and Paul J. K. Bruce†
Imperial College London, London, SW7 2AZ, United Kingdom

James A. Merrifield
Fluid Gravity Engineering Ltd., Emsworth, Hampshire, PO10 7DX, United Kingdom

In order to accurately predict the demise of a satellite during atmospheric re-entry, it is necessary to develop models which can predict heat fluxes to reasonably complex faceted shapes, including the peak heat fluxes which occur near corners and edges. Due to the limited number of detailed studies of hypersonic flows around faceted shapes, the development of such high fidelity models can be challenging. In order to help remedy this problem, this work uses 2D laminar CFD to investigate the Mach 5 flow around a square across a range of different Reynolds numbers. The results show that the flow has a strong dependence on Reynolds number. It is found that at Reynolds numbers above about 5×10^4 a separation forms on the top surface of the square, while at Reynolds numbers below this value the flow remains attached. The presence of separated flow significantly affects the heat fluxes along this surface. This, in addition to a number of other flow phenomena such as the peak heating rates immediately upstream and downstream of a sharp corner, are not accounted for by existing re-entry prediction tools, and therefore these methods are likely to predict incorrect heating rates. This could have a significant effect on estimates of ground casualty risks associated with re-entry events.

I. Nomenclature

a_c	=	speed of sound in a calculation cell
C_f	=	skin friction coefficient
C_p	=	pressure coefficient
d	=	characteristic molecular diameter
h	=	enthalpy
H_0	=	total enthalpy
Kn	=	Knudsen number
Kn_δ	=	boundary-layer Knudsen number
L	=	characteristic length
L_{sb}	=	separation bubble length
M	=	Mach number
M_e	=	Mach number at the edge of the boundary layer
N_A	=	Avogadro's number
P	=	pressure
q_0	=	stagnation point heat flux
q_{FR}	=	Fay & Riddell heat flux
q_{FR-FF}	=	equivalent flat-face Fay & Riddell heat flux
$\bar{q}_{top}$	=	average heat flux on the top face of a square
$Q_{corners}, Q_{body}$	=	heat transfer rate to the corners, body of a square
R	=	universal gas constant
Re	=	(free-stream) Reynolds number
Re_c	=	cell Reynolds number

*PhD Student, Department of Aeronautics, AIAA Student Member
†Senior Lecturer, Department of Aeronautics, AIAA Member

$\mathrm{Re}_{\infty,0}$	=	nose Reynolds number
Re_{θ}	=	momentum thickness Reynolds number
R_n	=	equivalent nose radius
s, z	=	coordinates tangential and normal to the surface
St	=	Stanton number
T	=	temperature
T_0	=	total temperature
U_∞	=	free-stream velocity
u, v	=	velocities in the s, z directions, respectively
u_i	=	inviscid velocity
Δy_{min}	=	height of the first cell from the wall
δ	=	boundary-layer thickness
ρ	=	density
ρ_∞	=	free-stream density
ρ_i	=	inviscid density
μ	=	viscosity
λ	=	mean free path

II. Introduction

Over more than half a century of human space-flight, approximately 6000 satellites have been placed in orbit around the Earth. Of these, fewer than 1000 are still operational, leaving a large number of decommissioned satellites in orbit [1]. Due to the limited availability of various Earth orbits, as well as the rapidly increasing risk of space debris, decommissioned satellites must be disposed of. Expired satellites are treated differently depending on their operational orbit. For example, geostationary Earth orbit (GEO) satellites are often placed in a graveyard orbit, typically a super-synchronous orbit well away from common orbits [2]. On the other hand, the orbits of decommissioned low Earth orbit (LEO) satellites are often left to gradually decay due to the atmospheric drag experienced in LEO, eventually resulting in an atmospheric re-entry. For smaller satellites, re-entry generally induces temperatures and forces large enough to destroy the satellite, with those parts that make groundfall posing an acceptably small casualty risk. However, for larger spacecraft the risk of ground casualties is non-negligible and it is generally accepted that space users have a duty to minimize the risks associated with re-entry events [3]. To this end, the European Space Agency (ESA) issued an instruction in 2014 that the casualty risk for any re-entry event should be no greater than 1 in 10 000 [4]. A number of other national space agencies, including NASA, also adhere to this figure [2].

In order to obtain an estimate of the ground casualty risk associated with a re-entry event, it is necessary to have a good understanding of the number of objects involved, their fragmentation and demise mechanisms, the effective cross-sections of the surviving components, their most likely locations as they hit the ground (in the case of controlled entries), as well as an accurate population density map of the Earth. It is therefore not surprising that there are significant errors associated with ground casualty risk calculations. In particular, there remains considerable uncertainty in predictions of the aerothermodynamic heating processes which occur during the initial stages of re-entry. This is largely due to the fact that satellite geometries are significantly different from most other re-entry bodies, typified by sharp corners, facets, and multi-scale structures. Compare, for example NASA's Upper Atmosphere Research Satellite (UARS) to the Apollo command module (Fig. 1).

Existing demise analysis tools use a variety of strategies in order to address this issue. So-called 'object-oriented' tools such as NASA's ORSAT [5] and ESA's DRAMA [6] use pre-correlated tumble-averaged total heating rates for specific geometric shapes such as plates, cubes or cylinders in order to predict heating to the individual components of the satellite. Some more general methods such as the 'spacecraft oriented' tool SCARAB [7] attempt to model heating to the entire spacecraft body by relating the stagnation-point heat flux to a characteristic body radius of curvature. The stagnation point value is then combined with a local inclination method for off-stagnation point fluxes. More recently, some demise analysis codes such as FOSTRAD [8] and PAMPERO [9] have adopted a new approach which relates aerothermal heating to a local radius of curvature. Others, such as SAM [10] use a weighted average of the Detra and Hidalgo stagnation point heating model [11], the Eckert reference temperature method [12], and Klett's data [13] for a cylinder in order to calculate heating to specific geometric shapes.

One issue with all of the methods described above is that very little high fidelity data for hypersonic aerothermal heating to faceted shapes has been published against which these heating models can be compared and validated. The

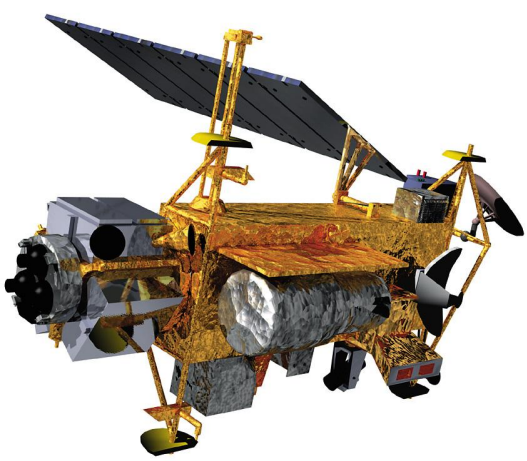

(a) The Upper Atmosphere Research Satellite (UARS). Image: NASA

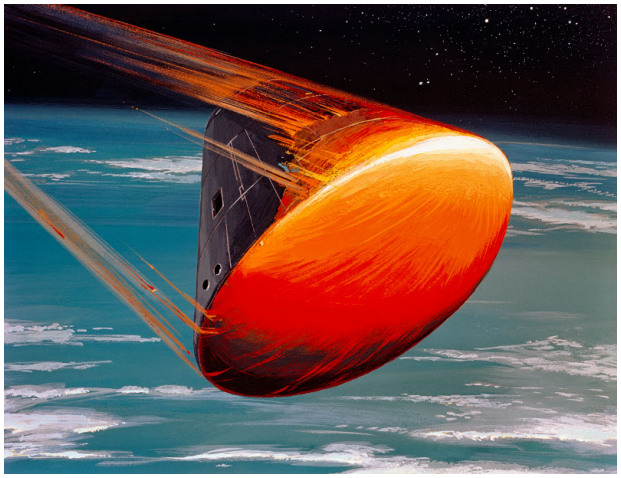

(b) Concept of Apollo 8 command module. Image: NASA Photo ID: S68-55292

Fig. 1 Comparison of the UARS satellite with the Apollo command module.

large majority of previous research into this subject was performed during the 1960s-1970s , when an interest in the re-entry behaviour of General Purpose Heat Sources (GPHS) drove some experiments into the heating rates experienced by faceted shapes in hypersonic flows. Most publications from this era, such as Refs. [13–17] considered heating rates to flat-ended cylinders, and largely neglected any detailed study of the flow near corners. The reports of Crosby & Knox [18], and Langanelli [19] provide some very preliminary experimental data of heating to a cuboid shape.

Ultimately, it is the strong expansions around corners and edges which are the most important differences between the heating to a blunt, rounded shape and a faceted shape. Through such expansions, the flow accelerates and the boundary layer thins, causing the local heat flux to increase beyond the stagnation point value. Beyond the obvious importance of understanding what the maximum heat flux to a body is, some recent studies have suggested that satellite fragmentation mechanisms are driven by failure of fasteners and glues rather than melting of body panels [20]. As these components are often located near corners and edges, fully understanding the heating rates at these locations is all the more important. The scope of this work is to analyse the 2D hypersonic flow-fields around a square using CFD. While only very basic in nature, such a geometry is highly representative of many satellite geometries. Section III introduces TINA, the CFD algorithm used for the simulations, and provides a description of the mesh used. Section IV describes numerical results, including basic validation procedures. The paper concludes with a discussion of these results in the context of existing demise models as well as experimental design.

III. Methods

A. Navier-Stokes Solver: the Thermochemical Implicit Non-Equilibrium Algorithm (TINA)

The Thermochemical Implicit Non-Equilibrium Algorithm (TINA) is a proprietary Navier-Stokes solver developed by Fluid Gravity Engineering Ltd (FGE) [21, 22], and is used for all of the simulations presented in this work. TINA employs a second-order accurate, point and line implicit, time marching algorithm in order to solve the compressible Navier-Stokes equations on a 3D structured grid. It uses the approximate Riemann solver in conjunction with flux limiters for the inviscid fluxes. In order to ensure non-oscillatory behavior near shock waves, the code uses a Total Variation Diminishing (TVD) shock capturing algorithm. At FGE, it is primarily used for supersonic and hypersonic Navier-Stokes calculations where non-equilibrium thermochemistry is important (although these features are not used for the simulations presented in this paper).

B. Mesh

The same 2-D mesh (Fig. 2) is used for all the simulations performed in this work. Created with the GridPro WS mesh generation software, the mesh is block-structured, with 1.84×10^5 cells, and a first cell height from the surface of

the square $\Delta y_{min} = 10^{-7}$ m. As a result the first cell Reynolds number, Re_c defined in Eq. (1), never increases beyond 2.23 in any of the simulations (see Table 1). Figure 2b also presents the surface-coordinate system used in the results.

$$\mathrm{Re}_c = \frac{\rho_c a_c \Delta y_{min}}{\mu_c} \tag{1}$$

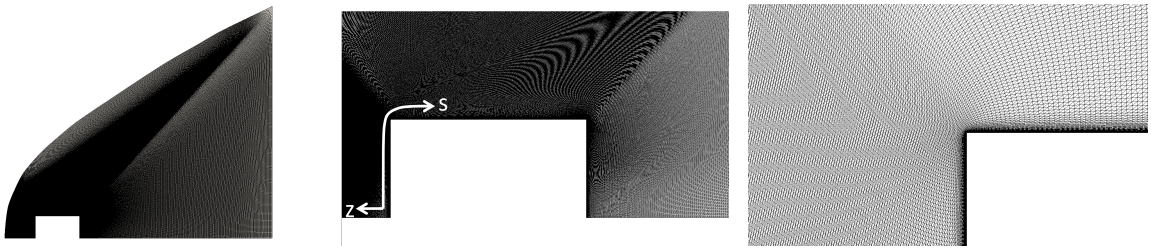

(a) Overview. **(b) Geometry detail.** **(c) Corner detail.**

Fig. 2 2D mesh used for the CFD simulations in this work along with the coordinate system used in the results.

IV. Results and Discussion

A. Flow Conditions

During a destructive re-entry, most objects undergo a catastrophic fragmentation at altitudes between 70-80 km due to the rapid increase in dynamic pressure at these altitudes. The exact altitude of this fragmentation is a significant factor in the size and number of fragments which hit the ground [6]. Therefore, when it comes to ground casualty risk estimates, understanding the state of the spacecraft in the period leading up to this fragmentation (between 80-120 km altitude) is very important. Due to the high velocities and low densities experienced by satellites in the upper regions of the atmosphere, re-entry flow-fields are typified by the unusual combination of high Mach numbers and low Reynolds numbers. Between the altitudes of 80-120 km, the flow around a satellite entering the atmosphere from LEO is typified by Reynolds numbers on the order of 10^3 while Mach numbers can be as high as 30. Another factor which must be considered when analysing re-entry flows is rarefaction. At the low densities experienced in the upper atmosphere the Knudsen number can be above 10^{-3}, which is often used as the value at which the continuum flow assumption is no longer valid [23]. For a perfect gas, these three dimensionless parameters are related by Eq. (2).

$$\mathrm{Kn} = \frac{\mathrm{M}}{\mathrm{Re}} \sqrt{\frac{\gamma \pi}{2}} \tag{2}$$

Due to the exponential relationship between atmospheric density and altitude, the Reynolds number (and therefore Knudsen number) can increase very rapidly during the initial stages of atmospheric entry. Therefore, this work examines the dependence on Reynolds number of the flow-field around a cuboid shape at constant Mach number. The exact conditions chosen for these simulations are based on conditions achievable in the Imperial College Supersonic Wind Tunnel (ICSWT). This will allow future experimental validation of these results. A combined blow-down/suck-down configuration with a working section of 150x150 mm, the ICSWT can achieve Mach numbers between 1.5-5, but with a Reynolds number range between $0.15 - 30 \times 10^6$ m^{-1}. This means that at the Mach 5 condition, a range of Reynolds numbers between 6.23×10^3 to 6.23×10^4 can be achieved for a 5 cm model. Furthermore, at these conditions, the free-stream density can be as low as 0.001 kg/m^3, which leads to Knudsen numbers of approximately 10^{-3} – just within the continuum flow regime while still being representative of real re-entry flows.

The conditions simulated in this paper are presented in Table 1. Simulations 1-10 presented in Table 1 correspond to conditions achievable in the ICSWT, while simulations 11-15 extend the Reynolds number through another order of magnitude in order to investigate flow behaviour at higher Reynolds values. Although Mach 5 is between four to six times smaller than typical re-entry Mach numbers, which can vary between 20-30, the concept of hypersonic Mach number independence suggests that dependence on Mach number might be weaker than dependence on Reynolds number, while any effects of flow reactions at these high Reynolds numbers can be investigated using more sophisticated

Table 1 Simulated flow conditions.

Case No.	M	Re	Kn	$\mathrm{Re}_{c,max}$	q_0, kW.m^{-2}	q_{FR-FF}, kW.m^{-2}
1	5	6.23×10^3	1.19×10^{-3}	0.0255	14.1	13.4
2	5	1.25×10^4	5.97×10^{-4}	0.0510	19.6	19.0
3	5	1.87×10^4	3.98×10^{-4}	0.0765	24.0	23.3
4	5	2.49×10^4	2.99×10^{-4}	0.102	27.4	26.9
5	5	3.11×10^4	2.39×10^{-4}	0.128	30.7	30.1
6	5	3.74×10^4	1.99×10^{-4}	0.153	33.6	32.9
7	5	4.36×10^4	1.71×10^{-4}	0.179	36.4	35.6
8	5	4.98×10^4	1.49×10^{-4}	0.204	39.0	38.0
9	5	5.61×10^4	1.33×10^{-4}	0.230	41.4	40.3
10	5	6.23×10^4	1.19×10^{-4}	0.255	43.7	42.5
11	5	1.09×10^5	6.83×10^{-5}	0.446	57.2	56.2
12	5	2.18×10^5	3.42×10^{-5}	0.892	80.4	79.5
13	5	3.27×10^5	2.28×10^{-5}	1.34	98.7	97.0
14	5	4.35×10^5	1.71×10^{-5}	1.78	114	112
15	5	5.44×10^5	1.37×10^{-5}	2.23	128	126

simulations later. Most importantly, it is judged that the value of experimental validation of these simulations outweighs this potential drawback.

B. Validation

As discussed in the Introduction, there has been little high quality data published for the flows considered, making validation a challenging problem. For a preliminary validation of of the numerical results, Table 1 shows comparisons between the simulated stagnation point heat fluxes to values given by the Fay and Riddell correlation [24]. The raw Fay and Riddell value for a cylinder q_{FR} must be transformed to the stagnation point value of an equivalent flat-faced stagnation point q_{FR-FF}. The flat faced value is calculated using the transformation suggested by Klett [13], who suggests that the flat-faced value is exactly half of the equivalent cylinder value. Results are presented in Table 1, and show good agreement, with no differences between the two values being larger than 5%, despite the simulated conditions lying slightly outside the range of validity of the Fay and Riddell correlation.

C. Flow-Field Structure

Figure 3 shows numerical Schlieren images of the flow immediately around the square geometry at Re= 6.23×10^3 (low), Re= 6.23×10^4 (intermediate), and Re= 5.44×10^5 (high). The contours are of normalised horizontal density gradient, and are all at the same scale. All three conditions show a compression on the windward surface, which becomes thinner as the Reynolds number increases, and a strong expansion around the windward corners. All three conditions also show an inclined pressure wave emanating from the top surface of the square. As Reynolds number increases, this pressure wave appears to strengthen. For the low and intermediate Reynolds numbers, this wave emanates from the windward corner of the square, whereas in the high Reynolds number case, it has moved downstream and an additional shock propagates from the windward corner. Examination of the shear stress (Fig. 4) on the square suggests the presence of a separation bubble on the top surface immediately downstream of this corner shock for the high Reynolds case. In fact, closer examination of Fig. 4b suggests the presence of a very small separation in the Re= 6.23×10^4 number case as well. In these, and all figures of surface values, the values are plotted against s/L, where s is the surface coordinate of the square (with its origin at the stagnation point) and L is the length of the square. The evolution with Reynolds number of the length and location of this separation is plotted in Fig. 5, which suggests that the separation first forms when $4.98 \times 10^4 < \mathrm{Re} \leq 5.61 \times 10^4$ and that L_{sb} tends to a constant value of approximately $L_{sb}/L = 0.55$ as Re is increased.

This separation behaviour is an example of "breakaway" or "shoulder" separation [25–27]. Although a sharp corner

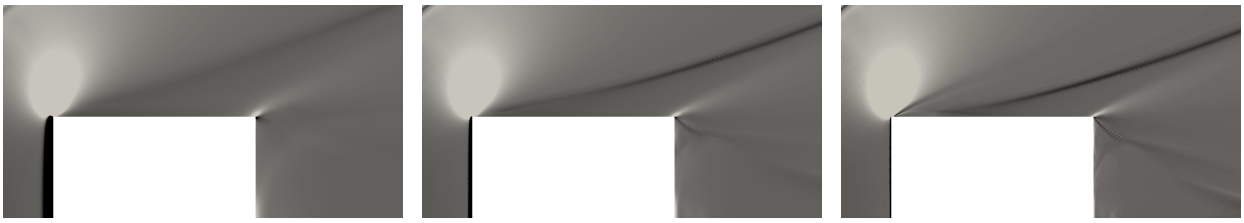

(a) Re = 6.23×10^3 **(b)** Re = 6.23×10^4 **(c)** Re = 5.44×10^5

Fig. 3 Numerical schlieren images of the post-shock flow-field around a square at Mach 5. Flow is from left to right.

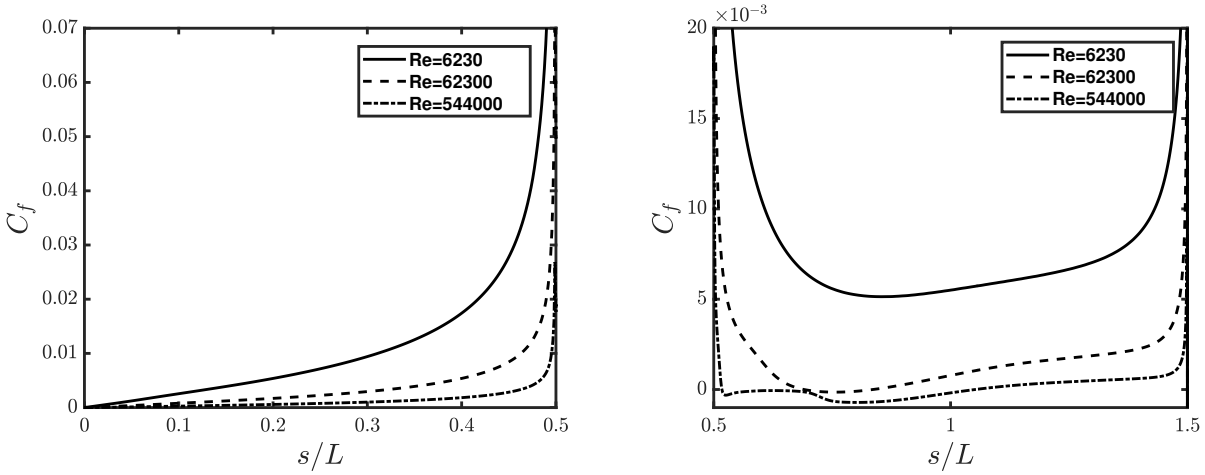

(a) Windward surface. **(b) Top surface.**

Fig. 4 Shear stress coefficient, C_f on a square in a Mach 5 flow.

in an incompressible flow will theoretically always induce a separation [28], this is not always the case for a supersonic (or hypersonic) flow. Previous discussions of shoulder separation in supersonic flows have provided a number of different interpretations of this behaviour. Wuerer and Clayton [27] described this separation as an inviscid process that is dependent on the maximum turning angle of the flow – when the angle of the geometry exceeds this value, the inviscid evacuated cavity downstream forms a viscous separation bubble, much like a supersonic wake. Later, other authors described the separation as a result of the balance of centrifugal and viscous forces through the corner expansion, and linked the separation with an adverse pressure gradient downstream of the separation point [26]. These numerical results support the latter two of these interpretations – all the simulations are performed at the same Mach number, and therefore the flows should all have the same turning angle. Due to their strong dependence on Reynolds number, the results instead suggest there is a significant viscous component to this phenomenon. Indeed, by examining the pressure distributions (Fig. 6) it is clear that the separation is associated with the adverse pressure gradient caused by flow recompression after the extremely strong expansion over the windward corner. Downstream of the separation, the flow passes through the recompression wave and continues to compress until it expands over the leeward side of the square. The results suggest that the boundary layer has not recovered to its zero pressure gradient profile before expanding over the leeward surface of the square. The next section provides an analysis of the boundary-layer behaviour observed in these simulations.

D. Boundary-Layer Behaviour

Due to the complex flow field structure, which includes shocks, expansions, and separations, as well as regions of strong heat flux, special care must be taken when defining the boundary-layer around the square. In this case, the

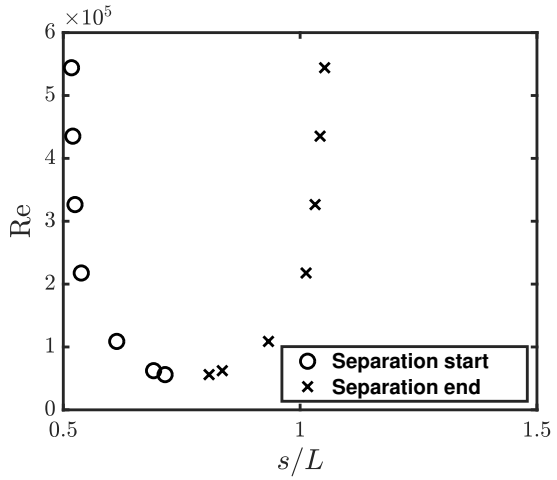

(a) Location of separation bubble.

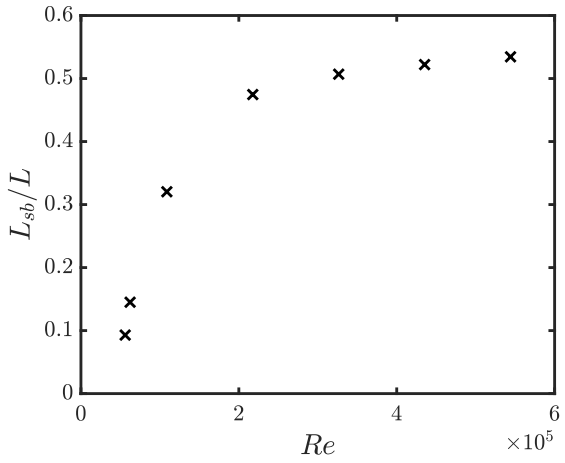

(b) Evolution of normalised separation bubble length.

Fig. 5 Separation bubble behaviour: dependence on Re.

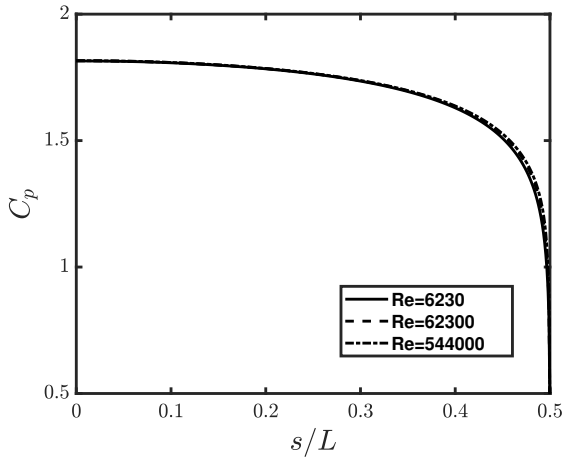

(a) Windward surface.

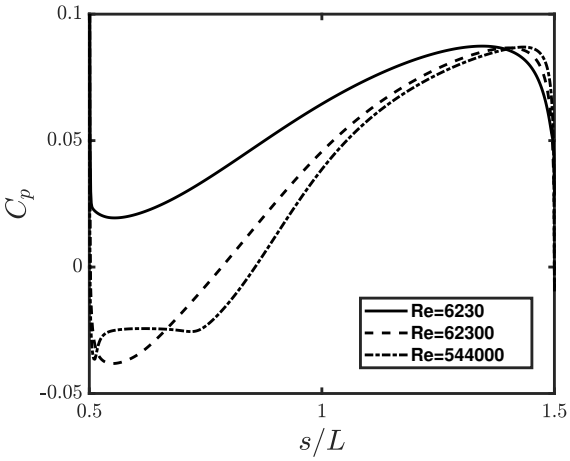

(b) Top surface.

Fig. 6 Pressure coefficient on a square in a Mach 5 flow.

boundary-layer height δ is defined as the location where the total enthalpy of the flow, $H_0 = h + |\mathbf{u}|^2/2$ returns to its free-stream value $H_{0,\infty}$. In this way, both the thermal and kinetic effects of viscosity are accounted for. The normalised boundary-layer height, δ/L is plotted in Fig. 7. The boundary layer can be seen to thin as it accelerates towards the windward expansion corner before more than tripling in thickness during recompression downstream of the corner.

$$\lambda_w = \frac{RT_w}{\sqrt{2}\pi d^2 N_A P_w} \tag{3}$$

An important parameter to consider is the wall Knudsen number Kn_w. Defined using the gas mean-free-path at the wall λ_w (defined in Eq. (3)) and using δ as the physical length scale, it shows the importance of rarefaction effects on the heat transfer to the body. Large values of Kn_w could indicate that the boundary-layer can not be modelled as a continuum and that rarefaction effects should be taken into account. This effect is expected to be especially important near the corners where a strong expansion causes a thinning boundary-layer while density decreases, and should increase Kn_w significantly. The results are plotted in Fig. 8. As expected, the maximum values occur near the windward corner where the boundary layer is thinnest. Furthermore, Kn_w increases above 0.001 for both the low and intermediate values

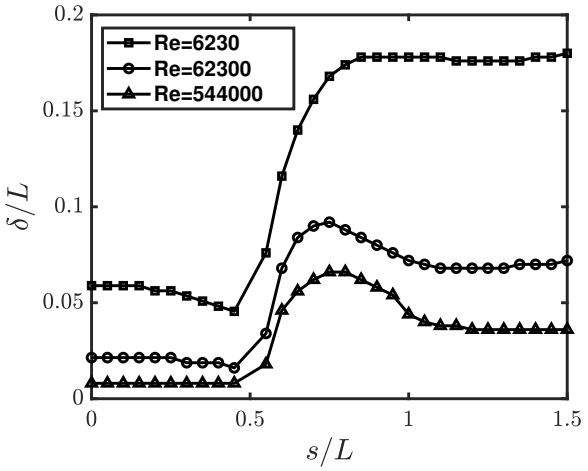

Fig. 7 Boundary layer height for three different values of Re

of Reynolds number, suggesting that, even if the free-stream Knudsen number is in the continuum region, local values can be well within the transition regime and could significantly affect heat flux calculations. This result should be taken into account when considering the heat transfer data presented below.

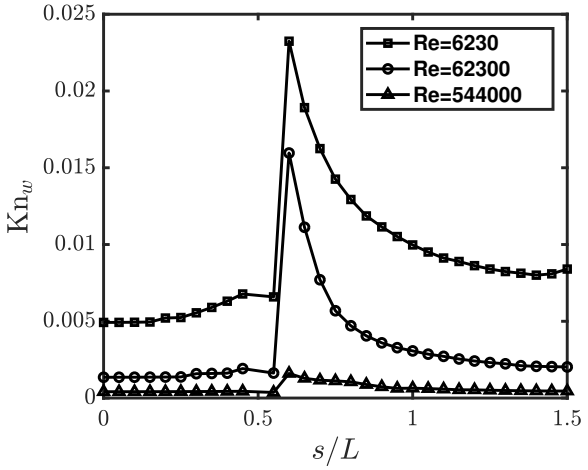

Fig. 8 Wall Knudsen number for three Re conditions.

Finally, in the analyses performed for this work, the boundary-layer is assumed to be laminar. Without experimental data, prediction of laminar-turbulent transition in the flow is very difficult. In order to gain some insight into the likelihood of laminar-turbulent transition, we will consider the behaviour of $\mathrm{Re}_\theta/\mathrm{M}_e$ along the surface of the square. This parameter is often used to predict laminar-turbulent transition in blunt-body flows, where values of over 100 are often used as a conservative transition criterion [23].

For a flat-plate boundary layer, the boundary layer momentum thickness, θ is defined as in Eq. (4). Such a definition is inappropriate for the boundary layer around the square as the strong pressure gradients present both streamwise and normal to the boundary layer can result in velocities within the boundary-layer being larger than the velocities outside. Furthermore, the inviscid, free-stream values of density and velocity are not constant as $z \to \infty$. We therefore use the momentum thickness definition of Bhanderi and Babinsky [29]. With this definition, the free-stream values of density and velocity are replaced by equivalent inviscid flow values ρ_i and u_i. The inviscid flow velocity u_i is defined using the gradient of the velocity at the edge of the boundary layer. Using this information, it is then assumed to vary linearly with distance to the wall, giving the inviscid wall velocity u_{iw}. The equivalent inviscid flow density ρ_i is then calculated

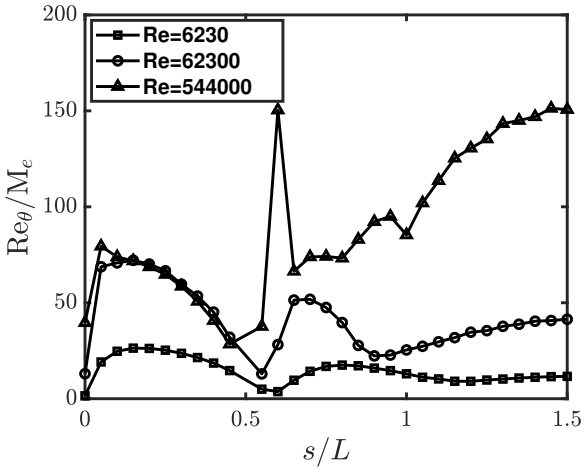

Fig. 9 Hypersonic boundary Layer transition metric for three different Re conditions. Re_θ is calculated using flow values at the boundary-layer edge.

by assuming the inviscid flow behaves isentropically from the edge of the boundary layer to the wall. In this case, the momentum thickness is defined as in Eq. (5), where $\rho_i(z)$ and $u_i(z)$ are both functions of z.

Values of $\mathrm{Re}_\theta/\mathrm{M}_e$ along the square are plotted in Fig. 9. The plot for the high Reynolds number case shows some coarseness and waviness on the top surface of the square. This is largely due to the sensitivity of Re_θ calculations to mesh fineness and boundary-layer height, especially in regions of strong separation. Although it is difficult to draw any conclusions using the absolute value of this parameter, it shows an increase around $s/L = 1$ for the high Reynolds number cases, suggesting that this could be a location where laminar-turbulent transition occurs. The turbulent flow downstream of this location would then significantly increase the heat fluxes from the values discussed below.

$$\theta = \int_0^\infty \frac{\rho(z)u(z)}{\rho_\infty u_\infty}\left(1 - \frac{u(z)}{u_\infty}\right) dz \tag{4}$$

$$\theta = \int_0^\delta \frac{\rho(z)u(z)}{\rho_i(z)u_i(z)}\left(1 - \frac{u(z)}{u_i(z)}\right) dz \tag{5}$$

E. Heat fluxes and Comparisons to Satellite Demise Heating Models

Normalised heat fluxes along the windward and top surfaces of the square are plotted in Fig. 10 for the same three low, intermediate and high Reynolds number values discussed above. Figure 10a shows the distribution of heat flux on the windward surface of the square. As expected, the heat flux increases beyond the stagnation point value as the flow approaches the corner. This well known phenomenon is due to the thinning of the boundary layer as the flow accelerates towards the corner expansion. In the case of a cylinder, Klett suggested that this trend could be modelled with Eq. (6) [13]. This relation is also plotted in Fig. 10a. The CFD data shows little dependence on Reynolds number and Klett's expression agrees remarkably well with all cases, except for the regions nearest the corner, where it overpredicts the heat flux for $0.34 < s/L < 0.48$ and underpredicts for $0.48 < s/L \leq 0.5$.

$$\frac{q}{q_0} = 1 + 0.6\left(\frac{x}{R_n}\right)^{3.3} \tag{6}$$

The effect of the separation bubble on heat flux is shown clearly in Fig. 10b. As the Reynolds number is increased, the value of normalised heat flux on the front half of the surface is depressed, decreasing by an order of magnitude below the cases where no separation is present. This is accompanied by an increase in the normalised heat flux on the latter half of the top surface. Despite the fact that heat fluxes acting on the top surface are an order of magnitude lower than the fluxes on the windward surface, their overall contribution to the total heat transfer is significant due to the much larger surface over which they exist. Figure 11 shows the variation of Q_{top}/Q_{body} with Reynolds number, where Q_{top}

and Q_{body} are the total heat transfer rates to the top surface and the entire geometry respectively. Aside from showing a clear dependence on Reynolds number, this ratio never falls below 0.2 for the Reynolds numbers simulated; this ratio will likely be even higher for 3D simulations due to the larger number of sides on a cube. Furthermore, if the boundary layer transitions to turbulence, as suggested by Fig. 9 for the higher Reynolds number cases, the heat fluxes will be higher still.

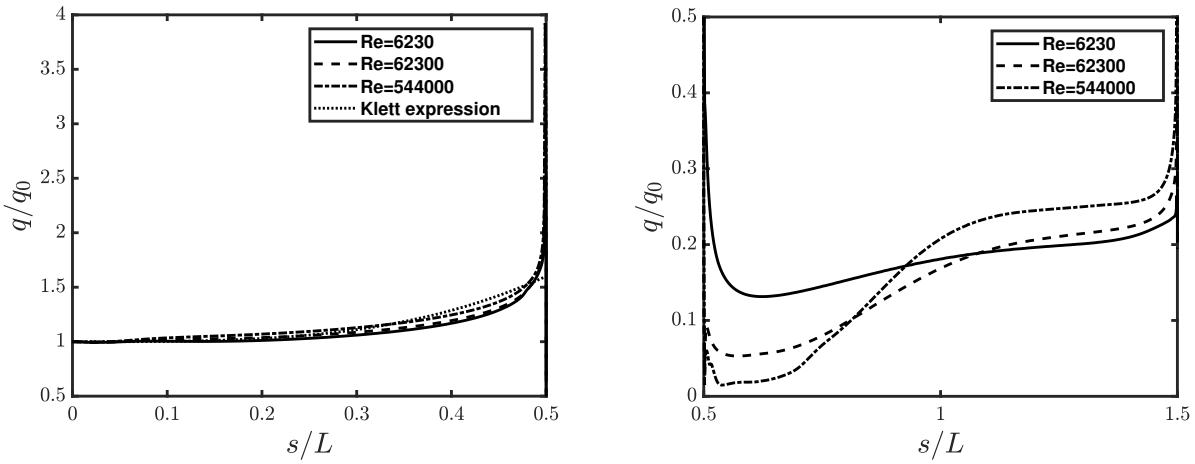

(a) Windward surface. **(b) Top surface.**

Fig. 10 Normalised heat flux to a square in a Mach 5 flow.

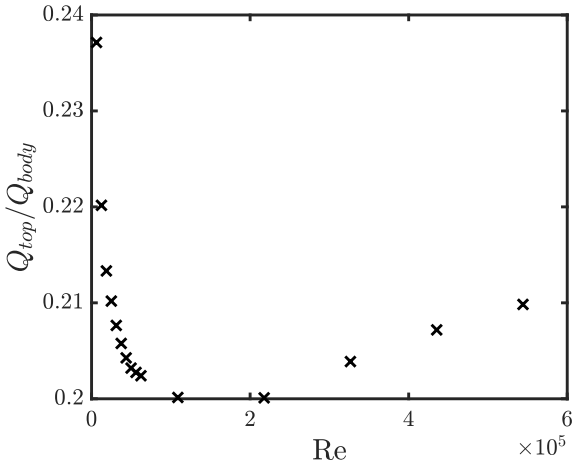

Fig. 11 Ratio of heat transfer to the sides to total heat transfer to body.

The other regions of high heat flux are the corners of the geometry. Figure 12 shows dependence of $Q_{corners}/Q_{body}$ on Re, where $Q_{corners}$ is the total heat transfer rate to the surface $0.1L$ either side of a corner. This value again shows a weak dependence on Reynolds number, with the heating rate near the corners of the geometry accounting for between 23-24% of the total heat transfer to the geometry.

$$\mathrm{St} = \frac{2.1}{\mathrm{Re}_{\infty,0}} \left(0.1 + 0.9\cos\theta\right) \tag{7}$$

$$\mathrm{Re}_{\infty,0} = \frac{\rho_\infty U_\infty R_n}{\mu\left(T_0\right)} \tag{8}$$

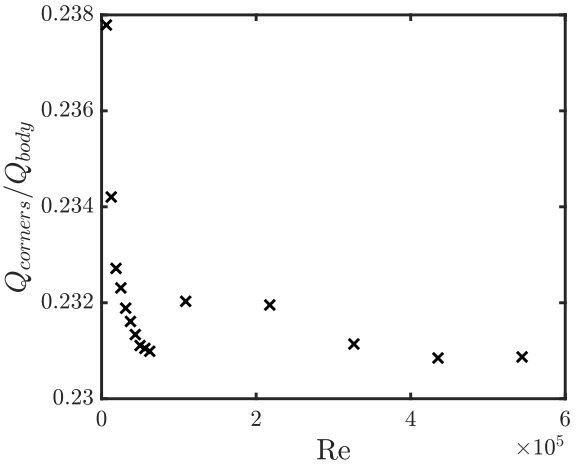

Fig. 12 Ratio of heat transfer near corners to total heat transfer to body.

As described in the Introduction, existing satellite demise tools use a number of approaches to predict heat fluxes to corners and off-stagnation point regions. One possible method for predicting off-stagnation point heat fluxes is the modified Lees method (Eq. (7), where $\mathrm{Re}_{\infty,0}$ is given by Eq. (8)). Used in the SCARAB demise analysis tool [7], this is a local inclination method based on the work of Lees [30]. The modified Lees method suggests that the normalised heat flux to a surface tangential to the free-stream flow is 10% of the stagnation point value, and that this value will show no dependence on Reynolds number. Figure 10b suggests that this model would significantly under-predict the heating rate to a square.

Figure 13 shows the ratio of the average heat flux to the top surface of the square normalised by the stagnation point heat flux. The ratio never drops below 16%. Another method of predicting off-stagnation point heating is to model the off-stagnation point regions as flat plates using the Eckert reference temperature method [10]. Not only does this method not take into account the possibility of the presence of a separation, Fig. 6b also shows that the boundary-layer on the top surface does not relax to its flat plate value. As a result, the heat transfer rate is significantly different from flat-plate heating models.

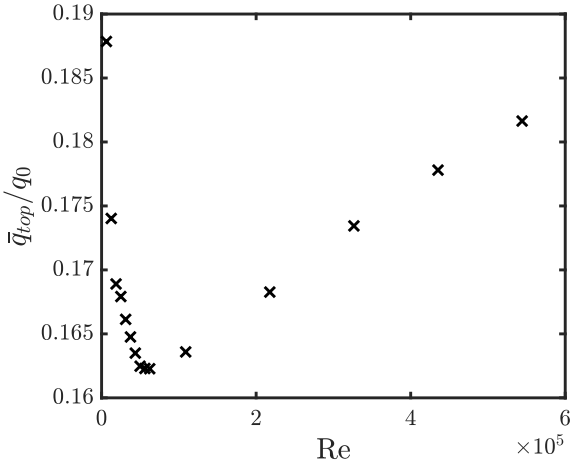

Fig. 13 Ratio of average heat flux on the top surface of square to the stagnation point heat flux.

V. Conclusions

In order to inform the development of future aerothermal heating tools for accurate predictions of satellite fragmentation and demise, 2D Laminar CFD studies were performed of the Mach 5 flow around a simple faceted geometric shape of unity aspect ratio at zero angle of attack. The simulations were performed over a Reynolds number range of $6.23 \times 10^3 \leq \mathrm{Re} \leq 5.44 \times 10^5$. The results suggest the following conclusions:

1) The hypersonic flow field around a 2D square shows a strong dependence on Reynolds number. For a Mach 5 flow, as the Reynolds number is increased, a separation bubble forms at $4.98 \times 10^4 < \mathrm{Re} \leq 5.61 \times 10^4$ and tends to a constant length of approximately $L_{sb}/L = 0.55$ as Re tends to infinity.
2) The presence of the separation bubble significantly affects heat fluxes on the body.
3) For all the Reynolds numbers simulated, after expanding around the windward corner of the square, the boundary-layer profile does not recover to its flat-plate profile before expanding through the leeward corner. It is therefore inappropriate to model the heating to this surface using flat-plate methods, such as the Eckert reference temperature method. A higher aspect ratio shape would be needed in order to make this approximation more valid.
4) Heating to the sides and corners of a square can account for 20-24% of the total heating rate to the body. This percentage is likely to be higher for 3D geometries. Furthermore, this percentage shows a weak dependence on Reynolds number. As a result the modified Lees method underpredicts heat fluxes to the sides of a square in a hypersonic flow by nearly 40%, although the exact value is a function of Reynolds number.
5) Due to the strong pressure gradients induced by the flow around a square shape, Knudsen effects can be important locally, even if the free-stream Knudsen number is in the continuum flow region.

Continuation of this work will include validation of the simulations with experimental data. 3D simulations and experiments on cubes and other faceted shapes will then provide a wider base of knowledge with which new heating models can be developed.

Acknowledgements

This work is funded and supported by Fluid Gravity Engineering Ltd., the European Space Agency (under NPI 480-2015) and the Engineering and Physical Sciences Research Council through the Imperial College Centre for Doctoral Training in Fluid Dynamics Across Scales.

References

[1] Trovatello, M., and Delaval, J., "Clean Space Twitter Q&A #AskESACleanSpace on Thursday 7 April 14:00 GMT," , 2016. URL `http://blogs.esa.int/cleanspace/2016/04/04/askesacleanspace`.

[2] NASA, "NASA-STD-8719.14A Process for Limiting Orbital Debris," , 2012.

[3] Merrifield, J., Beck, J., Markelov, G., Leyland, P., and Molina, R., "Aerothermal heating methodology in the spacecraft aerothermal model (SAM)," *7th IAASS Conference,*, Friedrichschafen, Germany, 2014.

[4] Dordain, J.-J., "ESA/ADMIN/IPOL(2014)2 - Space Debris Mitigation for Agency Projects," , 2014.

[5] Dobarco-Otero, J., Smith, R. N., Bledsoe, K. J., Delaune, R. M., Rochelle, W. C., and Johnson, N. L., "The Object reentry survival analysis tool (Orsat) version 6.0 and its application to spacecraft entry," *56th International Astronautical Congress of the International Astronautical Federation, the International Acadamy of Astronautics, and the International Institute of Spacwe Law*, Fukuoka, Japan, 2005.

[6] Martin, C., Cheese, J., Sanchez Ortiz, N., Bunte, K., Klinkrad, H., Lips, T., Fritsche, B., and Koppenwallner, G., "DRAMA Final Report," Tech. rep., European Space Agency, 2005.

[7] Koppenwallner, G., Fritsche, B., Lips, T., and Klinkrad, H., "SCARAB - A multidisciplinary code for destruction analysis of space-craft during re-entry," *Proceedings of the Fifth European Symposium on Aerothermodynamics for Space Vehicles*, Cologne, Germany, 2005.

[8] Mehta, P. M., Minisci, E., Vasile, M., and Walker, A., "An Open-Source Hypersonic Aerodynamic and Aerothermodynamic Modeling Tool," *8th European Symposium on Aerothermodynamics for Space Vehicles*, 2015.

[9] Annaloro, J., Omaly, P., Rivola, V., and Spel, M., "Elaboration of a New Spacecraft-Oriented Tool : Pampero," *Proceedings of the 8th European Symposium on Aerothermodynamics for Space Vehicles*, , No. 1, 2015.

[10] Merrifield, J., "Simplified Aerothermal Models for S / C Components (SAM): Executive Summary," Tech. Rep. July, Fluid Gravity Engineering Ltd, Emsworth, United Kingdom, 2015.

[11] Detra, R. W., and Hidalgo, H., "Generalized Heat Transfer Formulas and Graphs for Nose Cone Re-Entry Into the Atmosphere," *ARS Journal*, Vol. 31, No. 3, 1961, pp. 318–321.

[12] Eckert, E. R. G., "Engineering Relations for Heat Transfer and Friction in High-Velocity Laminar and Turbulent Boundary-Layer Flow over Surfaces with Constant Pressure and Temperature," *Transactions of the American Society of Mechanical Engineers*, Vol. 78, No. 6, 1956, p. 1273.

[13] Klett, R. D., "Drag coefficients and heating ratios for right circular cylinders in free-molecular and continuum flow from Mach 10 to 30," Tech. rep., Sandia National Laboratory, Albuquerque, NM, 1964.

[14] Kuehn, D. M., "Experimental and Theoretical Pressures on Blunt Cylinders For Equilibrium and Nonequilibrium Air at Hypersonic Speeds," Tech. rep., Ames Research Center, NASA TN D-1979, Moffett Field, CA, 1963.

[15] Matthews, R. K., and Eaves Jr, R. H., "Comparison of Theoretical and Experimental Pressure and Heat Transfer Distributions on Three Blunt Nosed Cylinders in Hypersonic Flow," Tech. rep., Arnold Engineering Development Center, AEDC-TR-67-148, Arnold Air Force Station, TN, 1967.

[16] Inouye, M., Marvin, J. G., and Sinclair, A. R., "Comparison of Experimental and Theoretical Shock Shapes and Pressure Distribution on Flat-Faced Cylinders at Mach 10.5," Tech. rep., Ames Research Center, NASA TN D-4397, Moffett Field, CA, 1968.

[17] Eaves Jr, R. H., "An Empirical Correlation of Pressure on Blunt-Nosed Cylindrical Afterbodies at Hypersonic Mach Numbers," Tech. rep., Arnold Engineering Development Center, AEDC-TR-68-82, Arnold Air Force Station, TN, 1968.

[18] Crosby, W. A., and Knox, E. C., "Heat Transfer and Static Stability Tests of the General Purpose Heat Source (GPHS) Configurations at Mach 8.0," Tech. rep., AEDC-TSR-80-V7, Arnold Air Force Station, TN, 1980.

[19] Langanelli, A. L., "Analytical and Experimental Heat Transfer and Flow-Field Prediction on a Rectangular Reentry Module," Tech. rep., SAI-067-81R-001, Science Applications inc., Wayne, PA, 1980.

[20] Soares, T., and Merrifield, J. A., "Characterization of Tests of Structural Joints Behaviour during Re-Entry," *4th International Workshop on Space Debris Re-entry*, ESOC, Darmstadt, Germany, 2018.

[21] Netterfield, M. P., "Hypersonic Aerothermodynamic Computations Using a Point-Implicit TVD Method," *1st European Symposium on Aerothermodynamics for Space Vehicles*, ESTEC, Noordwijk, the Netherlands, 1991.

[22] Netterfield, M. P., "Validation of a Navier Stokes Code for Thermochemical Non Equilibrium Flows," *27th AIAA Thermophysics Conference*, Nashville, TN, 1992.

[23] Anderson Jr., J. D., *Hypersonic and High-Temperature Gas Dynamics*, 2nd ed., AIAA, Reston, VA, 2006.

[24] Fay, J. A., and Riddell, F. R., "Theory of Stagnation Point Heat Transfer in Dissociated Air," *Journal of the Aerospace Sciences*, Vol. 25, No. 2, 1958, pp. 73–85.

[25] Kaufman II, L. G., Meckler, L., Hartofilis, S. A., and Weiss, D., "An Investigation of Hypersonic Flow Separation and Control Characteristics," Tech. rep., Air Force Flight Dynamics Laboratory AFFDL-TR-64-174, Wright-Patterson Air Force Base, Ohio, 1965.

[26] Kaufman II, L. G., Meckler, L., and Hartofilis, S. A., "An Investigation of Flow Separation and Aerodynamic Controls at Hypersonic Speeds," *Journal of Aircraft*, Vol. 3, No. 6, 1966, pp. 555–561.

[27] Wuerer, J. E., and Clayton, F. I., "Flow Separation in High Speed Flight A Review of the State-of-the-Art," Tech. rep., Douglas Aircraft Company Report SM-46429, Santa Monica, CA, 1965.

[28] Sychev, V. V., Ruban, A. I., Sychev, V. V., and Korolev, G. L., *Asymptotic Theory of Separated Flows*, Cambridge University Press, Cambridge, 1998.

[29] Bhanderi, H., and Babinsky, H., "Improved Boundary Layer Quantities in the Shock Wave Boundary Layer Interaction Region on Bumps," *35th AIAA Fluid Dynamics Conference and Exhibit*, Toronto, Canada, 2005.

[30] Lees, L., "Laminar Heat Transfer Over Blunt-Nosed Bodies at Hypersonic Flight Speeds," *Journal of Jet Propulsion*, Vol. 26, No. 4, 1956, pp. 259–269.